DOI: 10.1002/cphc.200500218

Apertureless Near-Field Vibrational Imaging of Block-Copolymer Nanostructures with Ultrahigh Spatial Resolution

Markus B. Raschke,*[a] Leopoldo Molina,[a] Thomas Elsaesser,[a] Dong Ha Kim,[b] Wolfgang Knoll,[b] and Karsten Hinrichs[c]

Nanodomains formed by microphase separation in thin films of the diblock copolymers poly(styrene-b-2-vinylpyridine) (PS-b-P2VP) and poly(styrene-b-ethyleneoxide) (PS-b-PEO) were imaged by means of infrared scattering-type near-field microscopy. When probing at 3.39 μm (2950 cm^{-1}), contrast is obtained due to spectral differences between the C–H stretching vibrational resonances of the respective polymer constituents. An all-optical spatial resolution better than 10 nm was achieved, which corresponds to a sensitivity of just several thousand C–H groups facilitated by the local-field enhancement at the sharp metallic probe tips. The results demonstrate that infrared spectroscopy with access to intramolecular dimensions is within reach.

1. Introduction

The chemical specificity that can be obtained from infrared (IR) vibrational spectroscopy had early on generated the desire for simultaneous spatial resolution. The combination with optical microscopy techniques, however, has remained a challenge. In far-field imaging, due to the long wavelength, it has proved difficult to exceed a resolution of several μm in the vibrational spectral region ($\lambda_{IR} = 3$–12 μm), even using coherent synchrotron or infrared laser sources.[1,2] Resorting to the optical near-field by extending the approach based on fiber tips as probes has also proved difficult. With the wavelength-related decrease in sensitivity imposed by waveguide cutoff and aperture transmission, 1-μm spatial resolution is seen as the practical limit.[3,4]

The potential for improved spatial resolution has been recognized by making use of the local-field enhancement and efficient scattering of nanoscopic metallic probe tips.[5–7] With the new technique of apertureless or scattering-type scanning near-field optical microscopy (*s*-SNOM)[8–10] an all-optical resolution of several nanometers in the visible has been demonstrated.[11–14] The expansion of this technique into the infrared spectral region has allowed the achievement of imaging contrast based on both molecular vibrational resonances[15–17] and optical phonons[18,19] with $\leq$80-nm spatial resolution.

This resolution is still insufficient for many chemical, biological and material-science applications, where it would be highly desirable, for example, to image surface chemical processes, submicron cellular features or semiconductor nanostructures, generating contrast relying on the intrinsic vibrational normal modes of the medium or low-energy-carrier excitations. In this study, the use of a refined tip design and better detection sensitivity allowed for an improvement of the spatial resolution based on vibrational contrast to less than 10 nm. With this superior resolution, vibrational imaging reaches—for the first time—the range of intramolecular dimensions. This will make possible molecular-level investigations of supramolecular species, organic nanostructures, colloids, biological membranes, and even single proteins.

Of these many interesting material systems to be studied, we demonstrate the new capabilities for the investigation of nanodomains of diblock-copolymer thin films. The connection between the chemically distinct units in block copolymers restricts the microphase separation of the respective chemical constituents, which results in spatially mesoscopic arrangements with a periodicity on the molecular-block length scale of 10–100 nm.[20,21] The complex microphase behavior has attracted much interest both concerning fundamental aspects[22–24] and because of the technological potential of block copolymers as functional materials for nanolithography, waveguides and sensor applications.[25,26] These investigations thus call for a high-resolution chemically specific imaging technique to visualize the spatial and chemical composition of the polymer.[27–29]

Here, a nanoscale surface analysis and identification of the domains formed by phase separation in thin films was achieved, choosing poly(styrene-*b*-2-vinylpyridine) (PS-*b*-P2VP) and poly(styrene-*b*-ethyleneoxide) (PS-*b*-PEO) as model systems. When probing at 3.39 μm (2950 cm^{-1}), contrast originates from

[a] *Dr. M. B. Raschke, L. Molina, Prof. Dr. T. Elsaesser*
Max-Born-Institut für Nichtlineare Optik und Kurzzeitspektroskopie
12489 Berlin (Germany)
Fax: (+49) 30-63921489
E-mail: raschke@mbi-berlin.de

[b] *Dr. D. H. Kim, Prof. Dr. W. Knoll*
Max-Planck-Institut für Polymerforschung
55128 Mainz (Germany)

[c] *Dr. K. Hinrichs*
ISAS—Institute for Analytical Sciences, 12489 Berlin (Germany)

differences in the spectral response of the C–H stretching vibrational modes between the two polymer constituents. Infrared *s*-SNOM thus provides direct information on the chemical composition. In addition, we show that thermally induced structural phase transitions can be studied in a spatially resolved fashion. The contrast obtained is discussed on the basis of a phenomenological model, and we present an outlook for the application of the method to other polymer and biological interfacial investigations.

2. Vibrational Contrast

The contrast in *s*-SNOM relies on the optical coupling between the probe tip and the sample, that is, how the light scattering of the tip is affected by a change of the dielectric function in its immediate environment.[6,30] In addition, the degree of near-field localization and enhancement of the optical field at the tip apex determines the resolution and sensitivity. For the geometry under consideration, this complex scattering problem can be simplified by describing the tip apex as a radiating optical dipole located only several nanometers above the sample. Specifically, the apex can be approximated as a polarizable sphere of radius r treated in the Rayleigh limit (i.e., $r \ll \lambda$) with dielectric constant ε_1, and located at a distance d with respect to the sample with dielectric constant ε_2. This model, which has been applied earlier to related geometries to describe, for example, the surface enhancement of Raman scattering,[31,32] can account for most experimental observations in *s*-SNOM.

The induced dipole moment $\boldsymbol{p}_1$ in the tip sphere, coupled to the sample in the presence of an illuminating plane wave $\boldsymbol{E}_0(\omega)$ is approximated by means of an effective polarizability α_{eff}:

$$\boldsymbol{p}_1 \equiv \alpha_{\text{eff}} \boldsymbol{E}_0 = \alpha \left(1 \pm \frac{\alpha\beta}{16\pi(r+d)^3} \right)^{-1} \boldsymbol{E}_0 \qquad (1)$$

where $\alpha = 4\pi r^3 (\varepsilon_1 - 1)(\varepsilon_1 + 2)^{-1}$ is the polarizability of the sphere and β is the moment of the virtual image dipole $\beta \boldsymbol{p}_1 = (\varepsilon_2 - 1)(\varepsilon_2 + 1)^{-1} \boldsymbol{p}_1$ in the sample to account for the boundary conditions at the interface.[33–35] The $+(-)$ sign corresponds to the electric field $\boldsymbol{E}_0(\omega)$, oriented parallel (perpendicular) to the tip axis. With the scattering intensity $I \propto |\alpha_{\text{eff}}^2|$, the change of scattered light due to the spatial variation of the optical properties of the sample thus provides the imaging contrast.

The local microphase separation in the block copolymers results in a lateral variation of the chemical composition with a micellar arrangement, as illustrated schematically in Figure 1 for the case of PS-*b*-P2VP. The optical properties of the respective polymer constituents were determined from spectroscopic ellipsometry, as will be discussed below. The resulting spectral variations of the complex refractive index $\tilde{n} = n + ik$ for polystyrene (PS) and poly-2-vinylpyridine (P2VP) are shown in Figure 1. For the infrared probe wavelength of 3.39 μm (2950 cm^{-1}) applied in our experiments dielectric constants of $\varepsilon_{PS} = 2.47 + 0.033\,i$, $\varepsilon_{P2VP} = 2.51 + 0.063\,i$, and $\varepsilon_{PEO} = 1.92 + 0.11\,i$ result. Together with $\varepsilon_{Au} = -435 + 84i$ for the gold tip,[36] Figure 2 shows a model calculation for the spatial variation of the effective polarizability of a tip with a 10-nm radius above

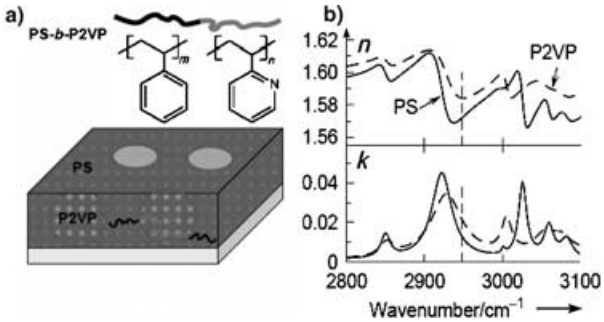

Figure 1. a) Chemical structure and schematics of the thin-film morphology of poly(styrene-*b*-2-vinylpyridine) (PS-*b*-P2VP) consisting of a regular micellar arrangement of P2VP cores with a PS corona. b) Frequency dependence of the real and imaginary part of the complex index of refraction $\tilde{n} = n + ik$ for the constituents of the diblock copolymers polystyrene (PS) and poly-2-vinylpyridine (P2VP) as derived from spectroscopic ellipsometry.

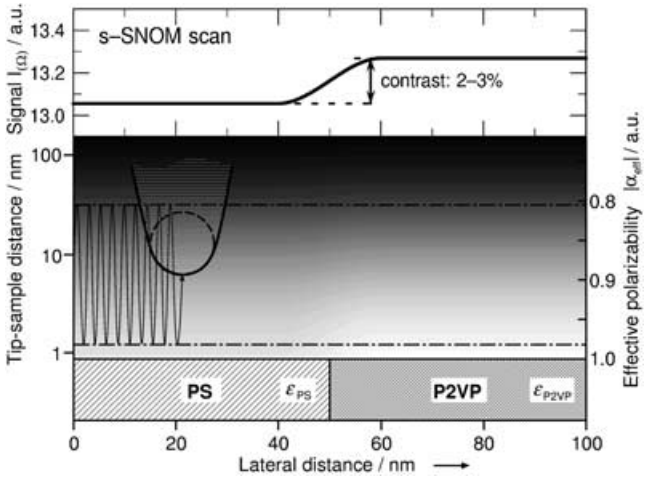

Figure 2. Generation of infrared vibrational contrast in *s*-SNOM: The spatial variation, vertically and laterally, of the effective polarizability of the tip is due to the dependence of the near-field optical coupling on the tip–sample distance and the spectral variation of the vibrational resonances (here, the C–H stretching probed at 2950 cm^{-1}, expressed as ε_{PS} and ε_{P2VP} for the different polymer constituents; gray scales: effective tip polarizability normalized to 1 at the P2VP surface). The oscillating tip projects the local optical tip–sample coupling into the radiating far field, ultimately carrying information on the optical properties of the sample with a spatial resolution only limited by the tip radius.

the sample. PS and P2VP were chosen as sample materials with a sharp lateral discontinuity. With the electric field polarized parallel to the tip axis, one finds a pronounced increase of the effective tip polarizability when approaching the sample surface. The resulting difference between PS and P2VP when the tip is in close proximity to the sample marks the contrast due to the specific values of ε_{P2VP} compared to ε_{PS}. To extract the corresponding tip-scattered signal contribution from the far-field background due to scattering from the tip shaft and sample roughness, a modulation of the tip–sample distance is applied and the near-field contribution is extracted from the synchronized signal component.[12,35] For a tip dither amplitude of 30 nm, the top panel of Figure 2 illustrates the expected

signal contrast and the correlation of the lateral resolution with the tip radius.

In contrast, for an applied field that is polarized perpendicular to the tip axis, the associated decrease in tip–sample coupling and thus in the effective tip polarizability would lead to a diminished signal intensity and reduced contrast of $\leq 1\,\%$. Similarly, with $n_{PS} = n_{P2VP} \simeq 1.59$ and $k_{PS} = k_{P2VP} \simeq 0$ in the visible spectral region, no contrast can be observed.

Experimental Section

The experimental setup is based on an atomic force microscope operating in noncontact mode (NC-AFM)[37] to control the distance between the probe tip and the sample and to obtain a topographic image simultaneously with the *s*-SNOM scan. The samples are studied under ambient conditions. For the light scattering a confocal epi-illumination and detection configuration is employed (Figure 3 a). Infrared radiation at 3.39 μm, provided by an HeNe laser,

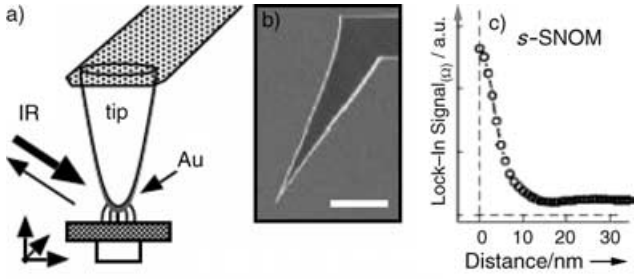

Figure 3. Scheme of the *s*-SNOM/AFM setup: a) epi-illumination and detection of tip-scattered 3.39-μm (2950-cm^{-1}) infrared light. b) Au-coated silicon cantilever tips used (scale bar 3 μm). c) Tip–sample-distance dependence of the *s*-SNOM signal indicating the local-field confinement determined by the tip apex radius and carrying information about the optical properties of the sample.

passes through a telescope, a Bereck compensator for polarization selection, a 50:50 beamsplitter and is collimated at 65° from the surface normal onto the tip by means of a Cassegrain objective (NA = 0.5, working distance = 23.2 mm). With 1.4 mW incident power this results in a fluence of $F \approx 2.8 \times 10^3\,W\,cm^{-2}$ at the tip within a focus diameter of $\varnothing \approx 8$ μm. The light emitted from the tip is collected through the same objective and detected by a mercury cadmium telluride detector (MCT, N_2(l)-cooled) with maximum detectivity of $D = 1 \times 10^{11}\,cm\sqrt{Hz}W^{-1}$ at the desired wavelength. The confocal geometry ensures minimal signal background. Sample scanning allows for constant illumination conditions of the tip and—unless noted otherwise— *p*-input polarization was chosen, that is, with the electric-field vector in the plane of incidence and thus parallel to the tip axis. In addition, the laser can be operated on the 632.8-nm emission line, which was used as a reference and for alignment. The objective, in combination with a tube lens and a CCD camera, provides a magnified tip image which allows for optimal beam alignment.

Two kinds of commercial silicon cantilevers (Ultralevers, Veeco Metrology Group, Santa Barbara and AdvancedTEC, NanoWorld AG, CH-Neuchatel) were used. In particular, the latter type, with the forward pointing tips shown in Figure 3 b, proved to be ideal for the experiments. For greater local-field enhancement and scattering efficiency the tips were coated with a nominally 30-nm-thick gold film. Performing the vacuum evaporation in the axial direction of the tip, given the large aspect ratio of the tips, results in a gold cap confined largely to the apex. With a resulting tip radius of $\leq$ 10–15 nm, as determined by scanning electron microscopy, this procedure mostly preserves the original apex radius of the silicon tips.

The time-harmonic vertical oscillation of the tip–sample distance at the cantilever resonance frequency in the range of 60–300 kHz (depending on the tip used and on the coating thickness) results in a corresponding modulation of the near-field interaction, as outlined above. Special attention was paid to noncontact AFM operation in the attractive mode to minimize distortions of the harmonic mechanical cantilever oscillation. Lock-in detection of the synchronized frequency component of the scattered signal at the fundamental or higher harmonic frequency thus allows for selection of the near-field contribution. With a dither amplitude of several tens of nanometers, the spatial signal variation is comparable to the length scale of the tip–sample coupling; yet, it is small with respect to the spatial far-field variations in the illumination area. In contrast to *s*-SNOM experiments performed at much shorter wavelengths in the visible, we find that the detection at the fundamental dither frequency is sufficient.[38] This is due to the comparably weak dependence of the far-field contribution and its interference on the tip–sample distance at infrared wavelengths. The corresponding tip–sample distance dependence of the tip-scattered light during approach to the PS-*b*-P2VP surface is shown in Figure 3 c. With field localization on a length scale given by the tip apex dimensions, this verifies the near-field signature. Here, zero distance is defined by the onset of damping of the cantilever oscillation induced by the van der Waals force interaction with the sample. The total DC signal ranges from $2\text{–}6 \times 10^{-4}$ of the incident intensity depending on the tip shape, roughness and slight variations in illumination conditions. For a tip oscillation amplitude of $\approx$30 nm, the modulated signal fraction amounts to $\approx 5 \times 10^{-3}$ near the sample, and is dominated by the contribution originating from the local tip–sample coupling with only a variable but small far-field background of $\leq 10\,\%$. Demodulation at the second harmonic of the dither frequency would further suppress this small residual far-field background, albeit at the expense of a decrease in sensitivity.[35,38]

The optical constants for the different polymer constituents were determined by means of spectroscopic ellipsometry in the spectral range: 2600–3500 cm^{-1}. Here, thin films of the corresponding homopolymers, spin-casted onto silicon-wafer substrates were used to derive the refractive index *n* and the absorption coefficient *k*, or equivalently, the components of the complex dielectric function $\varepsilon = \varepsilon' + i\varepsilon'' = (n + ik)^2 = \tilde{n}^2$. Figure 1 shows the result for *n* and *k* from the corresponding multi-Lorentzian fits to the measured ellipsometric parameters $\tan\Psi$ and Δ.[39,40] The spectra are characterized below 3000 cm^{-1} by the aliphatic C–H stretching vibrations, with the dominating antisymmetric CH_2 stretching mode at 2920 cm^{-1} and the weaker symmetric CH_2 stretching mode at 2850 cm^{-1}. In addition, for PS and P2VP, aromatic C–H stretching vibrations determine the response above 3000 cm^{-1}. Despite similar spectral characteristics, the differences with respect to spectral position, peak width, and amplitude, in particular of the antisymmetric CH_2 mode, suffice to provide strong enough contrast for *s*-SNOM probing at 2950 cm^{-1}.

Thin films of the block copolymers poly(styrene-*b*-2-vinylpyridine) (PS-*b*-P2VP, molecular weights $M_{n,PS} = 54\,900\,g\,mol^{-1}$, $M_{n,P2VP} = 18\,600\,g\,mol^{-1}$, polydispersity index 1.07, purchased from Polymer Source, Inc.) were prepared by spin-coating at 1000 rpm from 0.5 % (w/w) solutions in toluene onto native oxide-covered silicon wafers, resulting in a film thickness of $\approx$40–60 nm. Similarly $\approx$30-

nm films of poly(styrene-*b*-ethyleneoxide) (PS-*b*-PEO, $M_{n,PS}=19100\ g\,mol^{-1}$, $M_{n,PEO}=6400\ g\,mol^{-1}$, polydispersity 1.05, Polymer Source, Inc.) were prepared at 3000 rpm from 1% solution in benzene. With toluene as a selective solvent for PS, this results in a configuration of nanoscopic micelles with a PS corona and insoluble P2VP cores.[41–44] As both PS and PEO are soluble in benzene, cylindrical domains oriented normal to the substrate are formed in the case of PS-*b*-PEO.[45,46] Due to the rapid solvent evaporation the copolymers are kinetically trapped into these characteristic thermodynamically metastable configurations. The average domain lattice spacings L of the as-cut Ps-*b*-P2VP and PS-*b*-PEO films were determined by AFM[44] and small angle X-ray scattering[45], respectively. With average values of $L\approx40$ nm for both systems this characteristic length scale is larger than the respective bulk value, indicating that the spin-coated films are trapped in a non-equilibrium state.

3. Results and Discussion

Well-defined block-copolymer samples, with preconceived knowledge about the chemical identity of the domain composition, were selected to test and optimize the IR *s*-SNOM capabilities. In Figure 4, the simultaneously recorded topographic (a) and IR *s*-SNOM images at 3.39 μm (b) of a 300×300-nm^2 section of the PS-*b*-P2VP sample are presented. The topographic image reflects the characteristic surface morphology

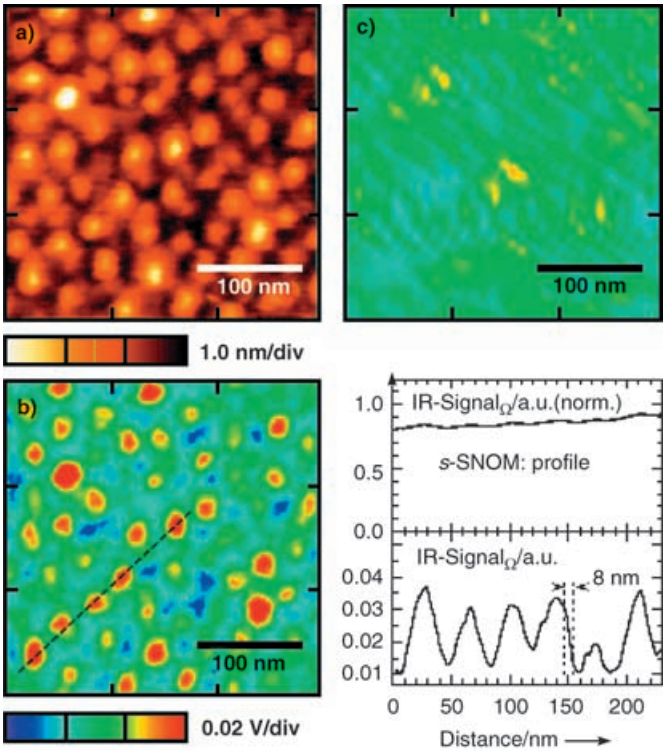

Figure 4. Simultaneously recorded a) topographic and b) infrared vibrational IR *s*-SNOM image at 3.39 μm (2950 cm^{-1}) of a PS-*b*-P2VP surface. The protruding regions corresponding to P2VP domains deliver a larger signal in accordance with their higher value for the complex dielectric constant. c) Corresponding *s*-SNOM image of a similar sample region recorded at a wavelength of 632.8 nm with no distinct contrast. d) IR *s*-SNOM spatial cross-section along the dashed line in (b) (upper trace: raw data; lower trace: normalized and far-field-corrected data). The lower trace indicates a spatial resolution as high as 8 nm.

with ordered protruded regions containing P2VP, distributed in the PS matrix. This nanophase separation manifests itself in the *s*-SNOM image in a corresponding spatial variation of signal intensities, with the more intense regions corresponding to the locations of the P2VP regions.

To visualize the low optical contrast between P2VP and PS the data were normalized line-by-line with respect to the intensity median after subtraction of a spatially slowly varying background. The latter is due to the residual background of typically 5–10%, as evident from the raw data cross-section (Figure 4d, upper panel) along the dashed line indicated in Figure 4b, and from comparing with the tip–sample distance dependencies of the signal (Figure 3c). This treatment, resulting in the signal trace shown in the lower panel, emphasizes the relative local-field-induced optical contrast between the two polymer constituents of order $0.8–2.5\times10^{-2}$ with respect to the signal maximum in this image, which is normalized to one. To achieve an adequate signal-to-noise ratio the data were typically acquired with a 0.05-Hz scan rate, which amounted to a total acquisition time of 1–2 h per image. They were typically recorded with a 1-s lock-in time constant, which resulted in a spatial integration over several nm. Higher-frequency noise, mostly originating from the data-acquisition electronics, was filtered.

From the raw data the observed contrast is significant, with a signal-to-noise ratio of ≈8:1. In accordance with the dipole coupling model, higher signal intensities are observed for the P2VP containing regions. In contrast, as shown in Figure 4c, when probing at 632.8 nm, that is, off the vibrational resonance, no definite optical contrast is observed in the near-field signal in corresponding *s*-SNOM images, despite higher detection sensitivity compared to the IR.

In general, a correlation between the topographic and *s*-SNOM images calls for special attention to possible sources of topographic artifacts. As will be discussed in detail elsewhere,[38] this can arise, for example, from a tip–sample distance-dependent interference and phase shifts of scattered light from the tip shaft, reaching the detector on different pathways, with and without reflection from the sample surface.[12,35] In our case this possible DC signal variation due to a phase change at $\lambda=3.39$ μm induced by a vertical height variation of even 10 nm (i.e., more than the 2 nm in the case of this polymer samples), however, would be less than 1×10^{-4} and thus below the detection sensitivity of our experiment. Instead, the observed signal dependence on the tip–sample distance, and the correlation of its decay length with the tip radius, provides direct evidence for the proper assignment of the detected signal. This, together with the absence of an attributable spatial signal pattern corresponding to *s*-SNOM in the visible at 632.8 nm, verifies that the contrast assignment is purely vibrational in origin.

In addition, a polarization dependence is expected to arise for two reasons: Firstly, as outlined above, due to the different degrees of optical coupling of the oscillating tip dipole to the sample, depending on its orientation; and secondly, the local-field enhancement at the tip apex is greatly reduced for perpendicular orientation of the electric field with respect to the

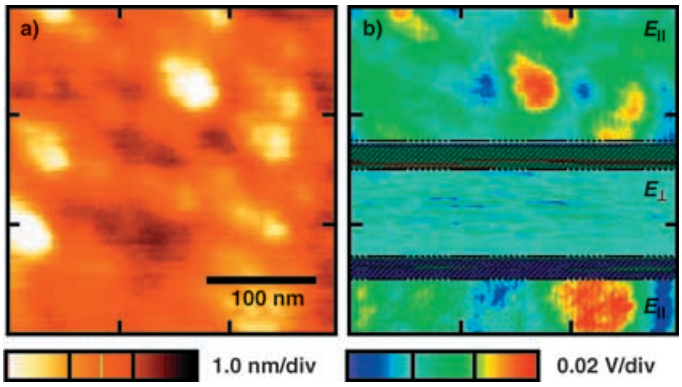

Figure 5. Simultaneously recorded a) topographic and b) IR *s*-SNOM image of PS-*b*-P2VP. During the scan the polarization of the incoming IR-radiation was changed from parallel to perpendicular with respect to the tip axis. The absence of any notable contrast for perpendicular polarization is due to both a reduced optical coupling and a weaker local-field enhancement.

tip axis.[47,48] Corresponding topography and infrared images recorded simultaneously are shown in Figure 5. Here, a minority region of the sample with slightly larger domains—possibly already indicating the onset of the thermal phase transition—has been selected to simplify this experiment. During the scan, the incident polarization is changed to *s*-polarization, that is, perpendicular to the tip axis and back to parallel. The perpendicular polarization is associated with a decrease in signal intensity and the absence of a notable spatial contrast. This can be attributed to both the weaker near-field coupling strength and a reduced local-field enhancement and corroborates the signal assignment and interpretation discussed above.

The morphology of thin PS-*b*-P2VP films formed after solvent evaporation presents a thermodynamically metastable configuration. Annealing above the glass transition temperature T_g leads to an equilibrium morphology by minimizing the total free energy. In thermal equilibrium, a morphology with cylindrical nanodomains oriented parallel to the substrate results (due to the specific interaction of the polymer blocks with the air and substrate interfaces). Here, the PS blocks are expected to segregate at the air interface.[49–51]

In the following we demonstrate the capability of IR *s*-SNOM for the spatially resolved study of the thermally induced structural phase transition. Figure 6 shows the result for the sample used for the previously discussed investigations (shown in Figure 4) after briefly heating to near the glass transition temperature followed by rapid cooling. As seen from the topographic scan, the surface smoothes significantly. Comparison with the associated *s*-SNOM image, however, shows that distinct morphological phases of PS and P2VP persist after this thermal treatment. Yet, except for selected topographic features (e.g., left circle marker) the former correlation between topography and the P2VP and PS domains has vanished (e.g., two right circle markers).

During the phase transition of a PS-*b*-P2VP film, the patterned morphology disappears due to segregation of PS at the air–polymer interface. In *s*-SNOM experiments this is associated with the vanishing of the optical contrast (result not shown). The above experiment thus shows the film captured in the ini-

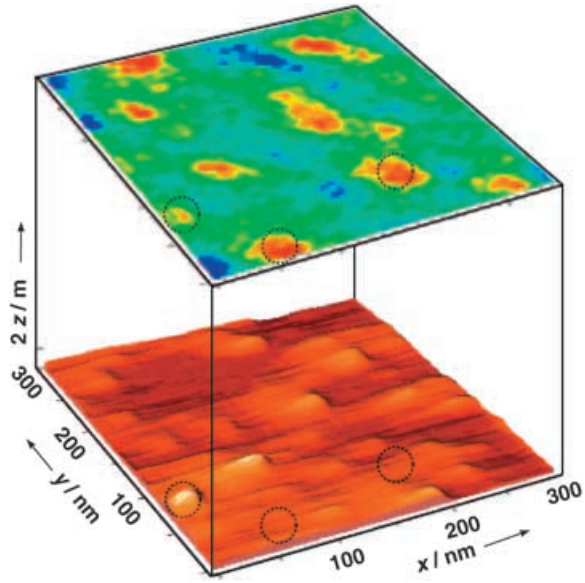

Figure 6. Topographic and corresponding IR *s*-SNOM image of PS-*b*-P2VP after several minutes of ex situ heating the sample to near the glass transition temperature followed by rapid cooling. Except for the few remaining P2VP protrusions the *s*-SNOM intensities no longer correlate with the topography. This corresponds to the initial stage of the phase-transition kinetics, with only minor vertical chain rearrangement and the persistence of the laterally phase-separated domains.

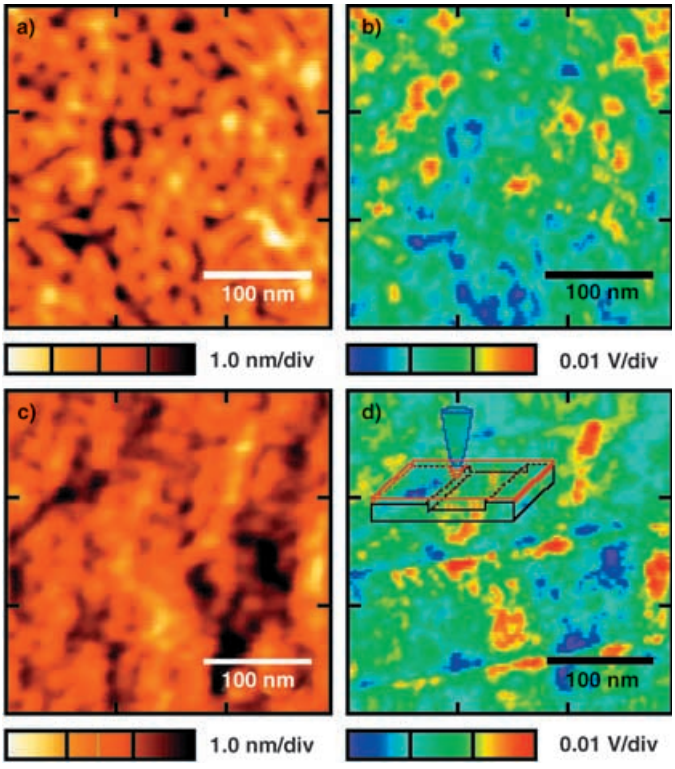

Figure 7. Topographic (a, c) and *s*-SNOM (b, d) images of two different regions of Poly(styrene-*b*-ethyleneoxide). While (b) shows a typical IR *s*-SNOM image, with a more intense signal originating from the PEO regions, two discontinuities occur in (d). These can be attributed to a vertical inhomogeneity of the sample, most likely a scratch in the underlying silicon substrate of this 30-nm-thick film. This emphasizes that the vertical material composition of the sample has to be considered at least on the length scale determined by the localization of the near-field of the tip apex.

tial stage of this phase transition when the film is still far from its thermodynamic equilibrium state. We thus identify the collapse of the micellar protrusions as the first step in the phase-transition kinetics. As there is only a small amount of vertical structural rearrangement associated with this step it is comparably fast. It is followed by the slower chain-diffusion process necessary to achieve full thermal equilibrium, which results after extended heating and which we find to be chemically homogeneous at the surface.

Figure 7 shows results of an *s*-SNOM investigation of a thin film of PS-*b*-PEO. Initially, after sample preparation the surface exhibits an array of nonuniform PEO domains. As PEO is hydrophilic, the film is susceptible to air humidity and can undergo some morphological rearrangement as the PEO expands. Due to the more pronounced difference between the dielectric constants of PS and PEO compared to the PS-*b*-P2VP system, one would expect an enhanced optical contrast with a larger *s*-SNOM signal for PEO. The moderate contrast observed, however, might indicate a PEO segregation at the polymer–air interface with the PS possibly partially buried by the PEO. This would be in accordance with the topographic image, which supports the interpretation of a chemically homogeneous surface possibly terminated by PEO.

Although already visible in the case of PS-*b*-P2VP, but more evident in this case, an apparent correlation of IR-scattered signal intensity with domain size is observed. Here, it needs to be considered that the tip-scattering response as a linear optical technique would not be surface-specific. Instead, the amount of sample medium contributing to the contrast would be given by the spatial extension of the local-field distribution around the tip apex and thus its penetration depth into the medium. Hence, one would expect that the vertical composition, at least on the length scale given by the tip apex radius, would contribute to the signal at any given tip position.

The effect of the vertical sample composition, the near-field localization at the tip apex and their interplay becomes very prominent in the data shown in Figures 7c and 7d. While in general the microscopic *s*-SNOM and topographic surface morphologies observed resemble that of the region investigated above, two distinct straight discontinuities are observed in the *s*-SNOM signal. This can only be understood assuming a subsurface feature, such as a scratch in the underlying silicon substrate. Although the film thickness of 30 nm would exceed the extension of the near-field from the tip apex, kinks and edges in the silicon substrate would give rise to localized and enhanced near-field distribution themselves given the low absorption of less than 0.5% of the incident far-field IR radiation by the 30-nm PS-*b*-PEO film. This field, in turn, can couple to the tip, giving rise to enhanced scattering intensities of the PEO domains in this region. The less planar morphology of the film developed in this sample region would corroborate this interpretation of a possible heterogeneity of the underlying substrate. This result emphasizes the need to consider the vertical composition of the sample carefully for proper *s*-SNOM interpretation, as discussed previously.[35]

From the signal intensity and contrast, together with the spatial resolution obtained, the amount of material responsible for the optical response can be estimated. Assuming that the local optical coupling decays spatially on the length scale of the lateral resolution, the signal would emerge from a confined probe volume of $\approx 10^3$ nm^3. With a density of ≈ 1.1 g cm^{-3} for the polymer, and taking the molecular structure into account, the signal would arise from $\approx 5\times 10^5$ aliphatic C–H oscillators. With a signal change of 1%, readily detectable in the scattering geometry, a difference of several thousand C–H groups would suffice to provide the contrast observed.

This sensitivity could be further improved by probing directly on resonance and by the selection of more chemically specific modes of the chemical compounds to be distinguished. In this respect, the carbonyl stretching bands (e.g., the amide I bands in proteins) are favorable due to their strong infrared response. The resulting sensitivity could suffice for probing intramolecular substructures, for example, particular functional groups of biological macromolecules.

4. Conclusions

In summary, we have demonstrated vibrational imaging of microphase separation in block-copolymer thin films with an unprecedented spatial resolution of ≤ 10 nm. Applying an apertureless near-field scattering configuration for light at 3.39 μm (2950 cm^{-1}), the dielectric contrast in the range of C–H stretching vibrations served for imaging the different chemical phases, making use of the strong field enhancement at the metallic probe tip. In contrast to surface-enhanced infrared absorption (SEIRA), the scattering technique applied here relies on the coupled tip–sample polarization in the range of a vibrational resonance. This infrared method is complementary to Raman techniques, that is., spontaneous Raman scattering and/or nonlinear coherent anti-Stokes Raman spectroscopy (CARS).[52,53] The large infrared polarizability results in pronounced scattering signals whereas the corresponding Raman techniques frequently require simultaneous resonance enhancement by electronic transitions. Our present experiments were performed with a fixed infrared wavelength. Future work will make use of tunable infrared sources to optimize the imaging contrast by selecting particular vibrational modes to develop the method into true infrared nanospectroscopy.

Acknowledgments

The authors thank Catalin Neacsu and Matthias Rang for stimulating discussions and Monika Tischer for tip preparation. Valuable support from Klaus-Jochen Eichhorn from IPF Dresden is acknowledged.

Keywords: block copolymers · IR spectroscopy · nanostructures · scanning probe microscopy · vibrational imaging

[1] J. A. Reffner, P. A. Martoglio, G. P. Williams, *Rev. Sci. Instrum.* **1995**, *66*, 1298.

[2] A. J. Sommer in *Handbook of vibrational spectroscopy: Mid-infrared transmission microspectroscopy* (Eds.: J. M. Chalmers, P. G. Griffiths),

Wiley, Amsterdam, **2002**, p. 1369; L. H. Kidder, A. S. Haka, E. N. Lewis in *Handbook of vibrational spectroscopy: Instrumentation for FT-IR imaging* (Eds.: J. M. Chalmers, P. G. Griffiths), Wiley, Amsterdam, **2002**, p. 1386.
[3] G. A. Marcuse, *Theory of dielectric optical waveguides*, Academic Press, San Diego, **1991**.
[4] D. Courjon, *Near-field microscopy and near-field optics*, Imperial College Press, London, **2003**.
[5] J. Wessel, *J. Opt. Soc. Am. B* **1985**, *2*, 1538.
[6] U. Ch. Fischer, D. W. Pohl, *Phys. Rev. Lett.* **1989**, *62*, 458.
[7] M. Specht, J. D. Pedarnig, W. M. Heckl, T. W. Hänsch, *Phys. Rev. Lett.* **1992**, *68*, 477.
[8] F. Zenhausern, M. P. O'Boyle, H. K. Wickramasinghe, *Appl. Phys. Lett.* **1994**, *65*, 1623.
[9] Y. Inouye, S. Kawata, *Opt. Lett.* **1994**, *19*, 159.
[10] A. Lahrech, R. Bachelot, P. Gleyzes, A. C. Boccara, *Opt. Lett.* **1996**, *21*, 1315.
[11] J. Koglin, U. C. Fischer, H. Fuchs, *Phys. Rev. B* **1997**, *55*, 7977.
[12] B. Knoll, F. Keilmann, *Opt. Commun.* **2000**, *182*, 321.
[13] R. Hillenbrand, F. Keilmann, *Phys. Rev. Lett.* **2000**, *85*, 3029.
[14] A. Hartschuh, E. J. Sánchez, X. S. Xie, L. Novotny, *Phys. Rev. Lett.* **2003**, *90*, 095503.
[15] B. Knoll, F. Keilmann, *Nature* **1999**, *399*, 134.
[16] B. B. Akhremitchev, S. Pollack, G. C. Walker, *Langmuir* **2001**, *17*, 2774.
[17] T. Taubner, R. Hillenbrand, F. Keilmann, *Appl. Phys. Lett.* **2004**, *85*, 5064.
[18] R. Hillenbrand, T. Taubner, F. Keilmann, *Nature* **2002**, *418*, 159.
[19] N. Ocelic, R. Hillenbrand, *Nat. Mater.* **2004**, *3*, 606.
[20] F. S. Bates, G. H. Fredrickson, *Annu. Rev. Phys. Chem.* **1990**, *41*, 525.
[21] I. W. Hamley, *The physics of block copolymers*, Oxford University Press, Oxford, **1998**.
[22] P. F. Green, T. M. Christensen, T. P. Russell, *Macromolecules* **1991**, *24*, 252.
[23] A. P. Smith, J. F. Douglas, J. C. Meredith, E. J. Amis, A. Karim, *Phys. Rev. Lett.* **2001**, *87*, 015503.
[24] A. Knoll, A. Horvat, K. S. Layakhova, G. Krausch, G. J. A. Sevink, A. V. Zvelindovsky, R. Magerle, *Phys. Rev. Lett.* **2002**, *89*, 035501.
[25] S. Förster, T. Plantenberg, *Angew. Chem.* **2002**, *114*, 712; *Angew. Chem. Int. Ed.* **2002**, *41*, 688.
[26] C. Park, J. Yoon, E. L. Thomas, *Polymer* **2003**, *44*, 6725.
[27] C. Marcott, G. M. Story, A. E. Dowrey, R. C. Reeder, I. Noda, *Microchim. Acta Suppl.* **1997**, *14*, 157.
[28] R. Bhargava, S.-Q. Wang, J. L. Koenig, *Adv. Polym. Sci.* **2003**, *163*, 137.
[29] M. J. Fasolka, L. S. Goldner, J. Hwang, A. M. Urbas, P. DeRege, T. Swager, E. L. Thomas, *Phys. Rev. Lett.* **2003**, *90*, 016107.
[30] W. Denk, D. W. Pohl, *J. Vac. Sci. Technol. B* **1991**, *9*, 510.
[31] J. Gersten, A. Nitzan, *J. Chem. Phys.* **1980**, *73*, 3023.
[32] A. Wokaun, J. P. Gordon, P. F. Liao, *Phys. Rev. Lett.* **1982**, *48*, 957.
[33] R. Ruppin, *Surf. Sci.* **1983**, *127*, 108.
[34] P. K. Aravind, H. Metiu, *Surf. Sci.* **1983**, *124*, 506.
[35] M. B. Raschke, Ch. Lienau, *Appl. Phys. Lett.* **2003**, *83*, 5089.
[36] D. W. Lynch, W. R. Hunter in *Handbook of optical constants of solids* (Ed.: E. D. Palik), Academic Press, Orlando, **1985**.
[37] The scanning probe microscope *AutoProbe CP-Research* from Veeco Metrology Group was employed and modified to allow for a stationary probe tip and improved optical access to the tip.
[38] M. Rang, C. C. Neacsu, L. Molina, M. B. Raschke, unpublished results.
[39] A. Röseler, *Spectroscopic infrared ellipsometry in Handbook of ellipsometry* (Eds.: H. G. Tompkins, E. A. Irene), William Andrew Publishing, Norwich, NY, **2005**, p. 763.
[40] K. Hinrichs, D. Tsankov, E. H. Korte, A. Röseler, K. Sahare, K.-J. Eichhorn, *Appl. Spectrosc.* **2002**, *737*, 56.
[41] J. C. Meiners, H. Elbs, A. Ritzi, J. Mlynek, G. Krausch, *J. Appl. Phys.* **1996**, *80*, 2224.
[42] J. P. Spatz, S. Mössmer, C. Hartmann, M. Möller, T. Herzog, M. Krieger, H.-G. Boyen, P. Ziemann, B. Kabius, *Langmuir* **2000**, *16*, 407.
[43] G. Kästle, H.-G. Boyen, F. Weigl, G. Lengl, T. Herzog, P. Ziemann, S. Riethmüller, O. Mayer, C. Hartmann, J. P. Spatz, M. Möller, M. Ozawa, F. Banhart, M. G. Garnier, P. Oelhafen, *Adv. Funct. Mater.* **2003**, *13*, 853.
[44] X. Li, P. Göring, E. Pippel, D. H. Kim, W. Knoll, *Macromol. Rapid Commun.* **2005**, *26*, 1173.
[45] Z. Lin, D. H. Kim, X. Wu, L. Boosahda, D. Stone, L. LaRose, T. P. Russell, *Adv. Mater.* **2002**, *14*, 1373.
[46] D. H. Kim, X. Jia, Z. Lin, K. W. Guarini, T. P. Russell, *Adv. Mater.* **2004**, *16*, 702.
[47] C. C. Neacsu, G. Steudle, M. B. Raschke, *Appl. Phys. A* **2005**, *80*, 295.
[48] C. C. Neacsu, G. A. Reider, M. B. Raschke, *Phys. Rev. B* **2005**, *71*, 201402.
[49] H. Hasegawa, T. Hashimoto, *Macromolecules* **1985**, *18*, 589.
[50] B. Collin, D. Chatenay, G. Coulon, A. Ausserre, Y. Gallot, *Macromolecules* **1992**, *25*, 1621.
[51] D. G. Walton, G. J. Kellogg, A. M. Mayes, P. Lambooy, T. P. Russel, *Macromolecules* **1994**, *27*, 6225.
[52] N. Anderson, A. Hartschuh, S. Cronin, L. Novotny, *J. Am. Chem. Soc.* **2005**, *127*, 2533.
[53] T. Ichimura, N. Hayazawa, M. Hashimoto, Y. Inouye, S. Kawata, *Phys. Rev. Lett.* **2004**, *92*, 220801.

Received: April 19, 2005

